

Effects of Non-symmetrical Current Distribution Controlled by Capacitor Placement in Loop Coils at 300 MHz MRI

Daniel Hernandez

Department of Biomedical Engineering, Gachon University, Incheon

Donghyuk Kim

Department of Health Sciences and Technology, Gachon University, Incheon

Yonghwa Jeong

Department of Health Sciences and Technology, Gachon University, Incheon

Taewoo Nam

Department of Health Sciences and Technology, Gachon University, Incheon

Kyoung-Nam Kim (✉ kyoungnam.kim@gachon.ac.kr)

Department of Biomedical Engineering, Gachon University, Incheon

Research Article

Keywords:

Posted Date: March 8th, 2022

DOI: <https://doi.org/10.21203/rs.3.rs-1402908/v1>

License:   This work is licensed under a Creative Commons Attribution 4.0 International License.

[Read Full License](#)

Abstract

In this work, we present a study on the effects of the non-symmetric electrical design of radiofrequency (RF) coils for magnetic resonance imaging (MRI) operating at ultra-high frequency (UHF). A typical loop coil used in MRI consists of symmetrically distributed capacitors along the coil; this design is able to produce uniform current distributions inside the coil. However, in UHF conditions, the magnetic flux density ($|B_1|$) field produced by this setup may exhibit field distortion, requiring a method of controlling the field distribution and improving the field intensity of the circular loop coil. The control mechanism investigated in this study is based on the position of the tuning capacitor in the circular coil. We performed comparisons against a reference coil that is based on a circular coil with four symmetrically distributed tuning capacitors. We performed electromagnetic (EM) simulations and MRI at 7 T to determine the effects of variations in the position of the capacitor and confirmed that unbalanced current distributions were created.

Introduction

The use of ultra-high-field magnetic resonance imaging (MRI) is desirable because of its capability of producing images with a higher signal to-noise ratio (SNR) [1, 2]. In principle, this is possible because more spins align in the presence of a stronger magnetic field, producing a stronger signal. When the main magnetic field strength is increased, the frequency at which the spins resonate also increases, as expressed by the Larmor frequency equation [3]. Therefore, the frequencies of operation of the transmission and reception of radiofrequency (RF) devices are also increased. However, increasing the frequency of operation signifies that the wavelength is reduced, which, in combination with the frequency dependency of the electrical properties of materials [4–6], reduces the effectiveness of the RF ($|B_1|$)-field inside the imaging target [7–11]. This results in field non-uniformity and the production of local hot spots of absorbed energy, as measured by the specific absorption rate (SAR) [12–14].

Creating an RF coil with uniform and low SAR is a challenge that has constantly been a topic of research. Several RF transmissions and receptors [15–17] have been proposed to address the occurrence of field non-uniformity. The use of high frequencies allows the application of antennas such as microstrips [18, 19], dipoles [20, 21], and monopoles [22], because the sizes of these devices, as determined by the wavelength, are acceptable and practical for use inside an MRI scanner within this frequency range. Recently, the concept of a “loophole” coil [23], which is a coil based on creating an unbalanced current distribution through modifications in the capacitor values along the coil, has been proposed. The loophole concept is based on inducing a loop coil to act as a dipole and has been demonstrated to be capable of producing higher field uniformity when used in a volumetric array configuration, and high resistance to loading effects, compared to reference and typical coils [24].

In this work, we present an empirical study on applying the concept of a loophole by creating a non-symmetric distribution of current on circular coils. In our study, we focus on modifying the position of the capacitor on a circular coil. The circular coil is equipped with a single tuning capacitor, the position of

which is changed along the coils in a radial form from its center and is indicated by the angle from the source. We performed electromagnetic (EM) simulations on coils with different capacitor positions and analyzed cases based on empty space and using a phantom. We also analyzed the coupling between pairs of coils with nonsymmetric capacitor positions by measuring the S21 parameters. Linear arrays with coils at a given capacitor position were also modelled, with the human spine as the examination target. We also developed loop coils, performed bench tests on the coupling, and obtained images of a phantom with a 7T MRI system.

Results

We performed a study on the effects of the angular position of the capacitor along the circumference of a loop coil. In the simulations and MRI experiments, it was expected that the non-uniform current distribution caused by the non-symmetrical capacitor position in the coil would improve the RF excitation ($|B_1^+|$)-field, and that this concept can be used to optimize the $|B_1^+|$ -field for particular applications. These studies included both simulations and MRI experiments. Because the amount of data to present was large, we used extracted line profiles, and rather than showing each $|B_1|$ -map, we plotted statistical values. For simplicity, we labeled the coils based on the angular positions of the capacitors; for example, the coil that had its capacitor at 45° was labeled as C45.

FDTD simulations of single element in empty space. A total of 24 simulations were performed with loop coils placed in an empty space. Each coil was excited to 300 MHz using a Gaussian pulse with a bandwidth of 600 MHz, and all simulations were normalized to an input power of 1 W. Figure 1 shows the computed surface current densities (J) of the selected coils. The absolute vector surface current density of the reference coil is shown in Fig. 1a. The maximum current density was produced by C15, as shown in Fig. 1b; this current density was higher than that of the reference coil. The surface current exhibited two bands of low intensity at 90° and 270° , which were caused by the change in the phase of the x component of the phase of the current density. Figure 1c–d shows the current densities for C90 and C180, respectively. C90 exhibited J with a higher intensity on the opposite side of the capacitor location. Despite the asymmetry of the J distribution, this coil produced the most uniform $|B_1^+|$ -field in the XY plane. On the other hand, a lower J distribution was computed for C180, which also had the lowest average $|B_1^+|$ -field. This coil had a J intensity that was lower than that of the reference coil; however, C180 was also a coil with a symmetrical capacitor-wire distribution.

A comparison between lower and high frequencies has been included in Fig. 1e–f, showing the J distributions for C45 when it was tuned to 300 MHz and 100 MHz, respectively. These simulations show the frequency dependency: because higher frequencies correspond to shorter wavelengths, they result in greater susceptibilities to changes in the position of the capacitor. At the same time, this is an opportunity to optimize the coil with focus on the $|B_1^+|$ -field in a desired area.

We computed the $|B_1^+|$ -field in empty space, which depicts slices at the center of the coil in the XY plane (Fig. 2a-i) and in the ZY plane (Fig. 2a-ii). To better visualize the performance of each coil, we obtained three-line profiles of the computed $|B_1|$ -field. The first profile (white line in Fig. 2a-i) was set 50 mm from the coil, and the results are shown in Fig. 2b-i. The second line profile (green line in Fig. 2a-i) was set at a larger distance, i.e., 200 mm, and the results are shown in Fig. 2b-ii. The third line profile is taken in the ZY plane (green line in Fig. 2a-ii) 50 mm from the coil, and the results are shown in Fig. 2b-iii. These line profiles show that the reference coil (blue solid line) had a less-than-average field strength compared with the other coils. At short and large distances, the coils with capacitors positioned at 15° and 345° exhibited higher field intensities, as depicted by the red solid, and dotted lines. The line profile graphs show an interesting characteristic, where the field intensity varied in accordance with the position of the capacitor: a higher intensity was produced when the position of the capacitor was closer to the source, whereas the lowest value was produced when the capacitor was at 180° . If these values are to be modeled, they will be approximated as a sum of cosine and sine:

$$f(\theta) = a_0 + a_1 \cos(\theta * w) + a_2 \sin(\theta * w), \quad (2)$$

where θ is the position of the capacitor given in degrees, and the coefficients a_0 , a_1 , a_2 , and w are dependent on the size of the coil, distance, and orientation of the line profile.

Another important aspect of this graph is how the reference coil compared with other coils; the performance of the reference coil was comparable to those of the coils with the capacitors positioned in the range 105° to 135° . It should be noted that, at this point, these inferences have been based only on empty-space simulations; in the presence of a dielectric material (loading case), the field pattern will be affected by the composition of that object. Nevertheless, this empty-space analysis revealed that it is possible to achieve a higher field intensity using coils of the same size and through simple modifications in the position of the capacitor.

In Fig. 2c, we describe the statistical results for the $|B_1|$ -field in empty space. We summarize the mean $|B_1^+|$ -field for each line profile. These figures show better correlations between the field intensity and the angular position of the capacitor. At short distances (Fig. 2c-i and Fig. 2c-iii), the reference coil performed better than eight other coil configurations only in terms of field strength. At large distances (Fig. 2c-ii), the reference coil performed better than only five of the coil configurations. We computed the coefficient of variance (CV), which is the standard deviation divided by the mean value, for each case, to determine the uniformity of the field. A lower CV value indicated that the samples were more uniform. For visualization purposes, we scaled the CV based on the maximum value for each distance such that the values could be fixed in the same plot as shown in Fig. 2d-i. This analysis is also interesting because it shows that depending on the application or desired field distribution, one can choose a coil configuration that would yield a more uniform field, either at short distances or at long distances. For example, C90 exhibited better field uniformity in the XY plane both at short and long distances from the coil. We also measured the focus of the field produced by each coil, and the difference in distance between the

maximum $|B_1^+|$ -field value and the center of the coil, as shown in Fig. 2d-ii. Positive values indicated that the maximum value of the field was oriented to the right, negative values indicated that the field was focused to the left, and a value close to 0 indicated a well-focused field. At short distances in the XY plane, the fields produced by coils C15 and C165 were more focused toward the center. At larger distances, the field produced by the coil with its capacitor at 90° was more focused toward the center compared to the fields produced by the other coils.

FDTD phantom simulations. We performed EM simulations on the same coil configurations but in the presence of the phantom. All simulations were performed using an excitation Gaussian pulse with a center frequency of 300 MHz and a BW of 600 MHz. Each coil was re-tuned and matched to 50Ω . The distance between the coils and phantom was 10 mm. Individual EM simulations were performed on each coil to acquire the $|B_1^+|$ -field. Figure 3 shows the $|B_1^+|$ -field for the selected coil configurations. Data analysis was performed using MATLAB (The MathWorks, Inc., Natick, MA, USA), and for data processing, the field maps were resampled to have the same matrix sizes, i.e., to $256 \times 256 \times 90$.

We compared the $|B_1^+|$ -field in the XY plane at the center of the coil between the reference coil (Fig. 3a-i left) and C315 (Fig. 3a-i right). We used the marked green line to create a field line profile, such that it would be easier to compare the coils with each other, as shown in Fig. 3b-i. The reference coil is indicated by the blue line. This graph shows an interesting pattern: the coils with their capacitors positioned between 15° to 150° exhibited higher field intensities focused on the left part of the field (negative x), with the highest intensity achieved by the coil with its capacitor at 75° . The coils with capacitors at 15° and 150° exhibited field intensities in this region similar to that of the reference coil. The coils that performed better in the right part of the field (positive x) were those with capacitors between 210° and 345° , with the highest field intensity in this region produced by the coil with its capacitor at 285° . The coil configuration that produced the best mean value for this line profile was C315. This indicated that it is possible to control the field focus through simple changes in the capacitor position. The $|B_1^+|$ -fields in the ZY plane for the reference coil (left) and C315 (right) are shown in Fig. 3a-ii, respectively. The line profile in Fig. 3b-ii shows that C285 and C270 exhibited the highest field intensities, whereas the reference coil exhibited a field intensity that was slightly better than the average.

A statistical analysis of the simulations involving the phantom is shown in Fig. 3c and 3d. The mean and standard deviation computed for the whole phantom (volume) for each coil configuration are shown in Fig. 3c-i and 3c-ii, respectively. This analysis revealed that coil C315 exhibited the highest field intensity, and that a total of 10 coil configurations resulted in better field intensities than that of the reference, with the lowest value achieved using C150. On the other hand, coil C240 resulted in the lowest standard deviation; moreover, eight coils resulted in better standard deviations than that of the reference coil. We segmented and created ROIs at each rectangle of the phantom to visualize the field patterns for each coil configuration. Figure 3d shows a representation of the mean value at each ROI for each coil configuration. The ROI number is shown on the y-axis, whereas the coil type is shown on the x-axis. We normalized each ROI (row) based on the maximum mean value among the coils to make it easy to

visualize which coil had the best performance at each ROI. We used a heat-color map to visualize these values, with a value of 100 representing the maximum field intensity on that row. This type of analysis could be used for designing loop coils with specific target zones or patterns. For example, the coil configurations from C15 to C150 exhibited higher field intensities toward the left, whereas the fields of C210 to C330 were more focused toward the right; this result also demonstrated that higher field penetration can be achieved using coil configurations C270 to C315. Of particular interest is ROI number 8, which was assigned electrical properties simulating those of CSF; the mean values at this ROI for all tested coil configurations are shown in Fig. 3c-iii. In this ROI, the coil with its capacitor positioned at 285° exhibited the highest mean value, which was 17% higher than that of the reference coil. This coil configuration was also demonstrated to be capable of producing the highest field intensity over a long distance from the coil, with most of the maximum values in the ROIs from 15 to 20, corresponding to the last row of the phantom.

When a transmission coil is analyzed, it is often desirable to show the SAR, and the performance of the magnetic field in relation to the SAR. In Fig. 4a, we show the 10 g-averaged SARs computed for the reference coil (left) and coil C180 (right), respectively. Figure 4b-i shows the maximum SAR for each of the coil configurations. The lowest SAR was exhibited by C180, whereas the highest was exhibited by C60. Normalization of the $|B_1^+|$ -field was performed via division by the square root of the maximum SAR. Figure 4a-ii show the normalized $|B_1^+|$ -fields for the reference and coil C345, respectively, whereas the mean value of the normalized $|B_1^+|$ -field is shown in Fig. 4b-ii. The results show that coil C345 exhibited the best performance, especially when compared with that of the reference coil.

FDTD simulations of array coil with phantom and Duke model. We also performed EM simulations on combinations of two coils to analyze the performance in terms of coupling [25, 26], as shown in Fig. 4c. For this analysis, we intentionally positioned the coils such that the distance between the coil centers was 65 mm. The objective was to determine if, at this distance, it is possible to obtain a better decoupling than that of the reference coil. We performed simulations with the following combinations: first, we performed simulations on pairs of coils with the same capacitor positions, and then performed simulations with pairs of coils with capacitors in opposite positions, e.g., 90° and 270°. Figure 4c-i shows the S21 parameters between coils with the same capacitor positions. As shown in the figure, the coils with capacitors positioned between 135° and 225° exhibited better decoupling than that of the reference coil. Specifically, coil C180 exhibited an S21 of -22.26 dB, whereas the reference coil exhibited an S21 of -17 dB. On the other hand, for the coils with capacitors in opposite positions, including the pairings with coils C90 and C180, the S21 parameters are shown in Fig. 4c-ii. For this type of configuration, coils C195 and C165 resulted in better decoupling than those of the other combinations; however, the values were still lower than that of the coil pair with C180.

We also performed EM simulations with a male human model (Duke), which consisted of more than 100 tissues, and positioned pairs of coils along the spinal cord. All simulations were performed using a Gaussian pulse with a central frequency of 300 MHz and a BW of 600 MHz, with a normalized input

power of 1 W. We performed a total of 24 simulations; each simulation was conducted on a coil array consisting of 12 elements. Each simulation involved one of the 23 coil configurations with capacitor positions ranging from 15° to 345° in 15° intervals, or the reference coil. For each simulation, the array was composed of coils of the same configuration, e.g., one simulation involved an array consisting only of coils in the C15 configuration, whereas another simulation involved an array consisting only of coils in the C90 configuration. The distance between the centers of the coils in the X direction was 65 mm. Figure 5a shows the $|B_1^+|$ -field normalized by the square root of the maximum SAR. For the $|B_1^+|$ -field in the XY plane, that of the reference coil array (Fig. 5a-i) is shown in the top row, whereas that of the C75 coil array (Fig. 5a-ii) is shown at the bottom; Fig. 5a show the XY planes at the centers of each pair of coils, as illustrated by the green lines. Coil C75 exhibited a higher field intensity than that of the reference coil array, both in the XY and ZY planes. In Fig. 5b, we summarize the statistical analysis for the entire volume and resized the matrix sizes of the simulations such that they are depicted with the same dimensions. Figure 5b-i shows the $|B_1^+|$ -field mean value for each of the coil arrays. The C75 coil array exhibited a higher field intensity than those of the other coil arrays, whereas the reference coil array exhibited the lowest field intensity. Furthermore, C180 exhibited the lowest mean value among the coils equipped with a single capacitor; incidentally, C180 was also a symmetrical type of coil. With regard to the uniformity, we computed the CV for each coil array and plotted the corresponding values in Fig. 5b-ii, which shows that C285 was the coil array that produced the most uniform field, which was approximately 60% better than that produced by the reference coil array. We also computed the maximum SAR_{10g} for the whole body, as shown in Fig. 5b-iii, which shows that C60 and C300 had the highest SAR_{10g} values, and that C180 had the lowest maximum SAR_{10g} . The results show that, in terms of the SAR, at least six of the coil arrays performed better than the reference coil array.

As an example of how this study can be applied to coil array design, we present a simple coil selection with the objective of improving the $|B_1^+|$ -field distribution on the spinal cord. The goal of this selection was to obtain a similar field intensity along the entirety of the spinal cord. The reason for this objective is that when a planar linear coil array is used, the field intensity is higher at the regions of the body that are closer to the coil, usually at approximately T6 and T11, whereas C1 to C4 would be subjected to lower field intensities because of the larger distance to the coils. The $|B_1|$ -field along the spinal cord could be optimized to be of a similar amplitude through selection of coil configurations that would yield a similar field intensity at every region of the spinal cord. To demonstrate this example, we performed a statistical analysis for each XY plane marked. We divided each region and computed the mean $|B_1|$ -field for each of the coil arrays, the results of which are shown in Fig. 5c-i. In this figure, the y-axis identifies the six regions corresponding to the position of the pair of coils, whereas the x-axis identifies the type of coil. For region 1, which corresponds to C1 to C4, the coil that exhibited the highest mean field value was C75, with an average of 0.033 μT . If we use this value as a reference, we can determine other coils that would have similar mean field values in the other regions. For regions 2 to 6, we can select the pairs of coils with C60, C240, C150, the reference coil, and C75, respectively. Each of these coils would have an approximate field value of 0.033 μT . We performed EM simulations using this selection of coil pairs to create an array. The

resulting $|B_1^+|$ -field is shown in Fig. 5c-ii and 5c-iii, including a comparison with the reference coil array. In this field map, we highlighted the value of the field equal to 0.02 μT , which was constant along the spinal cord for the case of the array of selected coils in comparison with the reference coil array. The field standard deviations computed for only the spinal cord for the reference and optimized coil arrays were 0.024 and 0.010 μT , respectively. This simple example demonstrated that it was possible to enhance the field pattern through the selection of coils with different capacitor positions.

Different capacitor placement in loop coils. We developed circular coils based on the dimensions of the simulations. We made one pair of coils for each capacitor position from 15° to 345° in 15° intervals, plus a pair of reference coils that had four capacitors evenly distributed. We tuned and matched the coils as shown in Fig. 6a-i. To simplify tuning and matching, we used variable capacitors. The coils were tuned to 297.3 MHz. The coils were placed on top of the phantom at the loading conditions. After tuning and matching, we tested the coupling between each pair of coils with the same capacitor positions. The S21 parameters are shown in Fig. 6a-i. We performed the test on three separation distances: 55, 60, and 65 mm between the centers of the coils, as shown in the top, middle, and bottom panels, respectively. Through this test, we intended to demonstrate that a number of the coils will exhibit better decoupling for different overlapping distances. The left column of Fig. 6a-i shows the S21 parameters for the reference coil, whereas the right column of Fig. 6a-i shows those for C45. Figure 6a-ii shows a summary of the S21 parameters for all the coils. According to the figure, for a distance of 55 mm, which corresponded to a high overlapping distance, the coils with the capacitor at 315° exhibited a low coupling of approximately -30 dB, in comparison to the reference coil, which demonstrated a coupling of -7 dB coupling. Most of the coils exhibited a lower coupling than that of the reference coils. When the distance between the coils was 60 mm (middle row in the figure), coils C45 and C255 exhibited a coupling of -20 dB, whereas when the distance was 65 mm (lower row), coil C30 demonstrated a coupling of -17 dB. In addition, we observed a number of special cases, where coils C105 and C285 exhibited couplings of -21 and -27 dB, respectively, when the distance between the coupled coils was 50 mm. Meanwhile, C300 demonstrated a coupling of -24.9 dB when the coil separation distance was 45 mm, whereas C90 exhibited a coupling of -20.6 dB when the coil separation distance was 40 mm.

Experiment implementation. We tested the performance of the coils by acquiring MR images in the presence of a phantom. The images were obtained using each coil equipped with a capacitor at each of the listed angular positions and with the reference coil. The images were captured using a 7T MRI scanner, with a gradient echo (GRE) pulse sequence, a repetition time of 300 ms, echo time of 4 ms, slice thickness of 3 mm, acquisition matrix of 256×256 , and flip angle of 30° . We repeated the experiment with each coil using the phantom, as described in the Method section. The images acquired using the selected coils are shown in Fig. 6b, showing the axial and sagittal views, respectively. We performed a comparison between the reference coil (Fig. 6b-ii), C45 (Fig. 6b-iii), and C240° (Fig. 6b-iv). The images are visualized with the same intensity window. For the reference coil, the images for ROIs 2 and 4 have lower intensities than those for C45. Meanwhile, the bottom row of the image, depicting the observations for C240, shows a higher intensity compared with those of the other two coils. We examined the image

intensity in each ROI of the phantom and visualized the summarized values in Fig. 6c-i, where the x-axis denotes the coil type, starting with the reference, and the y-axis denotes the ROI region. We used a heatmap representing the mean values; for easy visualization, we normalized the values to the maximum for each ROI, such that a row or ROI will show which coil had the best performance. According to the figure, the coil with its capacitor at 45° exhibited higher mean values than those of the other coils, whereas coil C240 also exhibited high intensity in its ROIs, according to the lower row of the figure. The statistical analysis for the sagittal view is shown in Fig. 6c-ii, which visualizes four regions and shows that C240 exhibited the highest mean value.

Discussion

This study demonstrated that the effect of the capacitor position along a loop coil can be considered for optimizing the designs of either transmission or reception coils for ultra-high frequencies. In this study, we performed simulations and experiments only for an operation frequency of 300 MHz, which could be applied for higher frequencies that are used in MRI systems with a stronger main magnetic field (B_0). Similarities between the mean values were observed in the simulations involving an empty space, phantom, and spine array. These plots show that, in the case of coil C180, the minimum field intensity was near that of symmetry, and because the capacitor was closer to the source, the field intensity was higher. Although this pattern changes depending on the loading condition, the graphs show a general concept of what can be expected. Similarly, the SAR values indicate that C180 can produce a lower SAR. There is also a relationship between the observations obtained from the simulation of couplings between two coils and the bench test on the developed coils, which reveal two local minima and one global minimum. Furthermore, the coils with the capacitors closer to the source demonstrated half of the dBs of the coils around C180, with the coils around C90 and C270 exhibiting the lowest dBs. This pattern also depends upon the fabrication of the coils, such as the vertical distance between the coils and matching board circuits. Nevertheless, this study suggests that higher overlapping distances can be achieved through simple changes in the capacitor position in the loop coil. This concept can also be applied to rectangular coils; however, in that case, the loophole concept may be more practical.

Conclusions

We present a study on the effects of changing the capacitor position in a loop coil, such that the findings can be applied to high-frequency applications in a 7T MRI scanner. We performed EM simulations and verified the simulation results using MR images. We also fabricated the coils and bench-tested the couplings of different pairings of coils. This study can be beneficial for applications where the $|B_1^+|$ field is optimized, the receiving coil arrays are characterized by different field patterns, the $|B_1^+|$ field is focused into a specific imaging region, or the SAR input into the patient is supposed to be reduced. This research can also be extended to higher frequencies and to the development of volumetric coil arrays. The concept of changing the capacitor position to alter the current distribution, as demonstrated in this study, also implies that breaking the symmetry of the resonators could enable the realization of target field patterns.

Methods

Based on the concept of the “loophole,” we modified the symmetry of the current distribution using a circular coil with only one tuning capacitor, the position of which was changed along the circumference of the coil. We configured multiple coils and varied the position of the tuning capacitor of the loop coil in intervals of 15° , starting from 15° from the source point, up to 345° . The reference coil was based on a loop coil equipped with tuning capacitors that are equally distributed around the coil, as shown in Fig. 7a. The reference coil had three tuning capacitors C_{sn} , where $n = 1, 2, \text{ and } 3$, located $90^\circ, 180^\circ, \text{ and } 270^\circ$, respectively, from the source. The coil had four segments of conductor line, which can be represented as series resistance R_{sn} and inductance L_{sn} . Capacitors and inductors are known for their ability to advance or delay the current in an RLC network. The total current can also be described as the sum of the incident I^+ and reflected current I^- [27]. If we apply segmented analysis at the capacitor position z , the current can be expressed as

$$I(z) = \frac{1}{Z_0} (V^+ e^{-\gamma z} - V^- e^{\gamma z}), \quad (1)$$

where V^+ and V^- are the incident and reflected voltages, respectively; Z_0 is the characteristic impedance of the conductor line; and γ is the propagation constant of the conductor line segment. With V^+ and V^- , we can compute the reflection coefficient Γ_n . For a symmetric distribution, if R_{sn} , L_{sn} , and C_{sn} are assumed to have the same values, the reflection coefficient view from the other side Γ_n^* will be the same, i.e., $\Gamma_n = \Gamma_n^*$, thereby maintaining a uniform current distribution, as is known. Now, when we modify the symmetry of the coil, as depicted in Fig. 7a–ii to 7a–iv, where the capacitor is positioned at different distances from the source, the conductor segments before the capacitor $\{R_{s1} \text{ and } L_{s1}\}$ will no longer be the same as $\{R_{s2} \text{ and } L_{s2}\}$, which results in a reflection coefficient relationship of $\Gamma_n \neq \Gamma_n^*$. This difference between the incident and reflected currents will modify the current distribution in the coil. In this study, we want to show that modifications in the current distribution could provide stronger and uniform $|B_1|$ -fields, and that the loop coil could be optimized to have specific field properties depending on the application and region of interest [28–30]. To verify this assumption, we performed numerical simulations [31–34].

FDTD Simulation setup. We performed simulations using a commercial finite-difference time-domain (FDTD) software (Sim4life, Zurich). We modeled a circular loop coil that included a source. For the reference coil, we included three tuning capacitors, whereas for each coil configuration that was studied, we included only one tuning capacitor. We performed simulations in empty space and with a loading phantom. For the empty-space simulation, the coils were 100 mm in diameter, whereas for the phantom and human-model analysis, the coils were 80 mm in diameter. The size difference of the coils was set to demonstrate that the concept can be applied to coils of different dimensions. The conductor line had a width of 5 mm and thickness of 0 mm, representing a perfect electric conductor (PEC). The gap between the source and capacitors was set to 3 mm. As mentioned previously, the position of the tuning capacitor along the circumference of the coil was varied from 15° to 345° in intervals of 15° . We used an automatic

method to create this model with the aid of a Python script and the Sim4life built-in functions to modify the design parameters. In addition, we devised a reference coil, which consisted of circular coils with a diameter of 80 mm, wire width of 5 mm, and three evenly spaced tuning capacitors, the positions of which were set to 90°, 180°, and 270°. Figure 7a shows the concept of the coils, a few examples of coils with capacitors at different positions, and the reference coil. Each coil was tuned and matched to 300 MHz and 50 Ω .

FDTD simulations in empty space. To demonstrate the performance of the concept, we first performed simulations on an empty space (without a phantom). We computed and acquired the current distribution of each coil and compared it with that of the reference and verified the $|B_1^+|$ -fields. The coils were excited using a Gaussian pulse with a center frequency of 300 MHz and bandwidth (BW) of 600 MHz. The capacitance of the tuning capacitors for the reference coil was 3.1 pF, whereas that for the asymmetric coils was 0.55 pF. It should be noted that, at least for the simulations, the same value of capacitance was used regardless of the position of the capacitor along the coil; however, this behavior changes when there is a loading material.

Phantom and human spine simulations. We also performed simulations using a phantom. As shown in Fig. 7b-i, the phantom had the shape of a cube with 20 cubic subdivisions. This phantom was selected to enable the inclusion of different tissue materials. Furthermore, we set the middle cube to act as cerebral spinal fluid (CSF), shown in blue, and the rest of the cubes as muscle tissue, shown in yellow. The use of the subdivision is also useful for automatic segmentation and region of interest (ROI) assignment. The ROIs were labeled with corresponding numbers, which will be used later for analysis. The separation material between the ROIs was set to be plexiglass. The electrical properties of the CSF (blue box) were set to a conductivity of 2.22 S/m and permittivity of 72.734; the muscle tissue was set to have a conductivity and permittivity of 0.77 S/m and 58.2, respectively [33]. The plexiglass was set to have a conductivity and permittivity of 0.0025 S/m and 2.6, respectively. These values were obtained from a database provided by the software. The phantom had a size of 170 × 170 × 170 mm³, whereas each cube had a size of 30 × 40 × 170 mm³. With this phantom, we performed simulations on each single coil and analyzed the coupling performance of the coil configurations, which were combined in pairs, as shown in Fig. 7b-ii.

We also performed simulations using a human model, known as the Duke model, provided by simulation software [36]. This model contains over 100 tissues and organs with electrical properties that correspond to the frequency of the operation. We used this model to test the coils in the examination of the spinal region by making linear arrays of coils with different capacitor positions. The simulations involved six pairs of coils: the first pair of coils was located between vertebrae C1 and C3, the second between C4 and C7, the third at T1 and T5, the fourth at T6 and T8, the fifth between T9 and T11, and the sixth at T12, L1, and L2, as shown in Fig. 7b-iii and 7b-iv. Each pair involved all 23 combinations of capacitor positions.

7T MRI experiments and phantom development. The RF coils were developed using a flexible copper material, with special cuts at the capacitor positions. We developed a total of 48 coils, which are shown in

Fig. 7c-i. We used these coils to acquire MRI images and to study the coupling behavior of nearby coils. The MRI experiments were performed using a 7T MRI scanner (Magnetom, Siemens AG, Berlin, Germany) at 300 MHz. We created a phantom based on a simulation model following the tissue selection. We used data from a past study [37] to select the corresponding electrical properties of the phantom. The electrical properties were implemented using a mixture of water, agar, sucrose, and NaCl. Figure 7c-ii shows the phantom and the placement of the coils for analysis.

Declarations

Acknowledgements

This study was supported by the Basic Science Research Program through the National Research Foundation of Korea (NRF) funded by the Ministry of Education (2021R1C1C1010003) and supported by Institute for Information & communications Technology Promotion(IITP) grant funded by the Korea government(MSIP) (No. 2021-0-00490, Development of precision analysis and imaging technology for biological radio waves)

Author contributions

D.H. conceived the concept of the study and performed EM simulations, data analysis, and writing. Y.J., T.N., and D.K. developed the materials and performed bench tests, experiments. K.N.K. supervised the project and document editing. All authors have reviewed the manuscript.

Additional information

Competing interests

The authors declare no competing interests.

Data availability

The datasets used and/or analyzed during the current study available from the corresponding author on reasonable request.

References

1. Vaughan, J. T. *et al.* 7T vs. 4T: RF power, homogeneity, and signal-to-noise comparison in head images. *Magn. Reson. Med.* **46**, 24–30 (2001).
2. Uğurbil, K. Imaging at ultrahigh magnetic fields: History, challenges, and solutions. *Neuroimage* **168**, 7–32 (2018).
3. Slichter, C. P. *Principles of magnetic resonance* (Vol. 1) (Springer Science & Business Media, 2013).
4. Ibrahim, T. S., Hue, Y. K. & Tang, L. Understanding and manipulating the RF fields at high field MRI. *NMR Biomed.* **22**, 927–936 (2009).

5. Seo, J. K. *et al.* Electrical tissue property imaging using MRI at DC and Larmor frequency. *Inverse Probl.* **28**, 084002 (2012).
6. Zhang, X., Zhu, S. & He, B. Imaging electric properties of biological tissues by RF field mapping in MRI. *IEEE Trans. Med. Imag.* **29**, 474–481 (2010).
7. Vaughan, T. *et al.* 9.4 T human MRI: preliminary results. *Magn. Reson. Med.* **56**, 1274–1282 (2006).
8. Park, M., Noh, H. & Park, N. Mitigation of B₁₊ inhomogeneity for ultra-high-field magnetic resonance imaging: hybrid mode shaping with auxiliary EM potential. *Sci. Rep.* **10**, 1–8 (2020).
9. Hwang, Y., Noh, H., Park, M., Lee, J. & Park, N. B₁₊ homogenization in 7T MRI using mode-shaping with high permittivity materials. Preprint at <https://arxiv.org/abs/1911.05313> (2019).
10. Schmidt, R. & Webb, A. Improvements in RF shimming in high field MRI using high permittivity materials with low order pre-fractal geometries. *IEEE Trans. Med. Imag.* **35**, 1837–1844 (2016).
11. Van de Moortele, P. F. *et al.* B₁ destructive interferences and spatial phase patterns at 7 T with a head transceiver array coil. *Magn. Reson. Med.* **54**, 1503–1518 (2005).
12. Seginer, A., Furman-Haran, E., Goldberg, I. & Schmidt, R. Reducing SAR in 7T brain fMRI by circumventing fat suppression while removing the lipid signal through a parallel acquisition approach. *Sci. Rep.* **11**, 1–3 (2021).
13. de Greef, M., Ipek, O., Raaijmakers, A. J., Crezee, J. & van den Berg, C. A. Specific absorption rate intersubject variability in 7T parallel transmit MRI of the head. *Magn. Reson. Med.* **69**, 1476–1485 (2013).
14. Zhu, Y., Alon, L., Deniz, C. M., Brown, R. & Sodickson, D. K. System and SAR characterization in parallel RF transmission. *Magn. Reson. Med.* **67**, 1367–1378 (2012).
15. Hernandez, D. & Kim, K. N. A review on the RF coil designs and trends for ultra high field magnetic resonance imaging. *Investig. Magn. Reson. Imaging* **24**, 95–122 (2020).
16. Elabyad, I. A., Herrmann, T., Bernarding, J. & Omar, A. Combination of travelling wave approach and microstrip transceiver coil arrays for MRI at 7T. *IEEE MTT-S International Microwave Symposium* (2011).
17. Connell, I. R., Gilbert, K. M., Abou-Khousa, M.A. & Menon, R. S. MRI RF array decoupling method with magnetic wall distributed filters. *IEEE Trans. Med. Imag.* **34**, 825–835 (2014).
18. Jasiński, K. *et al.* A volume microstrip RF coil for MRI microscopy. *Magn. Reson. Imaging* **30**, 70–77 (2012).
19. Bogdanov, G. & Ludwig, R. Coupled microstrip line transverse electromagnetic resonator model for high-field magnetic resonance imaging. *Magn. Reson. Med.* **47**, 579–593 (2002).
20. Connell, I. R. & Menon, R. S. Shape optimization of an electric dipole array for 7 tesla neuroimaging. *IEEE Trans. Med. Imag.* **38**, 2177–2187 (2019).
21. Raaijmakers, A. J., Luijten, P. R. & van den Berg, C. A. Dipole antennas for ultrahigh-field body imaging: a comparison with loop coils. *NMR Biomed.* **29**, 1122–1130 (2016).

22. Kausar, A. Z., Reutens, D. C., Weber, E. & Vegh, V. Monopole antenna array design for 3 T and 7 T magnetic resonance imaging. *PLoS One* **14**, e0214637 (2019).
23. Lakshmanan, K. *et al.* The “loopole” antenna: a hybrid coil combining loop and electric dipole properties for ultra-high-field MRI. *Concepts Magn. Reson. Part B Magn. Reson. Eng.* **2020** (2020).
24. Fujita, H., Zheng, T., Yang, X., Finnerty, M. J. & Handa, S. RF surface receive array coils: the art of an LC circuit. *J. Magn. Reson. Imaging* **38**, 12–25 (2013).
25. Lu, M., Gore, J. C. & Yan, X. Over-overlapped loop arrays: a numerical study. *Magn. Reson. Imaging* **72**, 135–142 (2020).
26. Kumar, A., Edelstein, W. A. & Bottomley, P. A. Noise figure limits for circular loop MR coils. *Magn. Reson. Med.* **61**, 1201–1209 (2009).
27. Branin, F. H. Transient analysis of lossless transmission lines. *Proc. IEEE* **55**, 2012–2013 (1967).
28. Bitton, R. R. *et al.* Evaluation of an MRI receive head coil for use in transcranial MR guided focused ultrasound for functional neurosurgery. *Int. J. Hyperth.* **38**, 22–29 (2021).
29. Fujita, H. New horizons in MR technology: RF coil designs and trends. *Magn. Reson. Med. Sci.* **6**, 29–42 (2007).
30. Hardy, C. J. *et al.* 32-element receiver-coil array for cardiac imaging. *Magn. Reson. Med.* **55**, 1142–1149 (2006).
31. Chen, J., Feng, Z. & Jin, J. M. Numerical simulation of SAR and B/sub 1/-field inhomogeneity of shielded RF coils loaded with the human head. *IEEE Trans. Biomed. Eng.* **45**, 650–659 (1998).
32. Perez, M., Hernandez, D., Michel, E., Cho, M. H. & Lee, S. Y. A tool box to evaluate the phased array coil performance using retrospective 3D coil modeling. *J. Korean Soc. Magn. Reson. Med.* **18**, 107–119 (2014).
33. Ibrahim, T. S., Lee, R., Baertlein, B. A., Yu, Y. & Robitaille, P. M. Computational analysis of the high pass birdcage resonator: finite difference time domain simulations for high-field MRI. *Magn. Reson. Imaging* **18**, 835–843 (2000).
34. Jin, J. M. *et al.* Computation of electromagnetic fields for high-frequency magnetic resonance imaging applications. *Phys. Med. Biol.* **41**, 2719 (1996).
35. Gabriel, C., Gabriel, S. & Corthout, Y. E. The dielectric properties of biological tissues: I. Literature survey. *Phys. Med. Biol.* **41**, 2231 (1996).
36. Christ, A. *et al.* The Virtual Family—development of surface-based anatomical models of two adults and two children for dosimetric simulations. *Phys. Med. Biol.* **55**, N23 (2009).
37. Duan, Q. *et al.* Characterization of a dielectric phantom for high-field magnetic resonance imaging applications. *Med. Phys.* **41**, 102303 (2014).

Figures

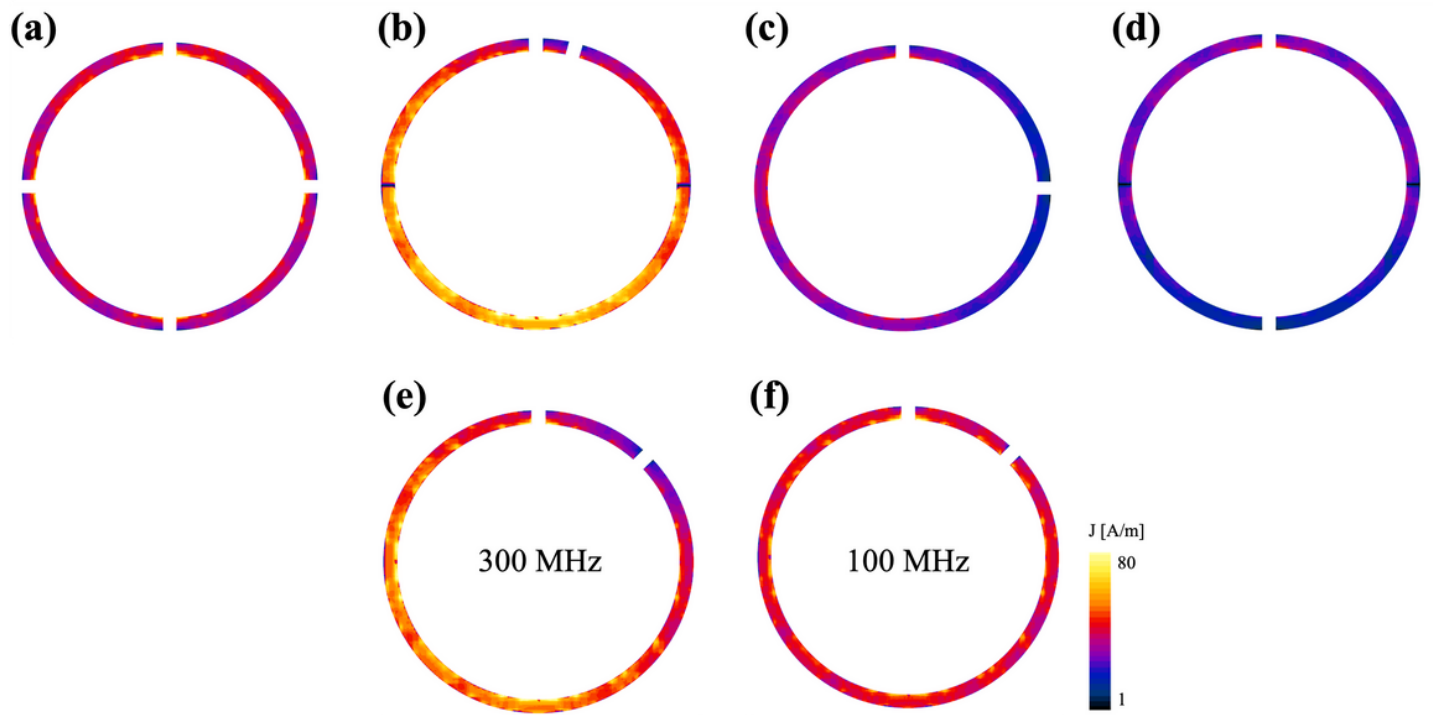


Figure 1

Current densities of (a) reference coil, and of coils with capacitor positioned at (b) 15°, (c) 90°, and (d) 180°; and at 45° when excited at (e) 300 MHz and (f) 100 MHz.

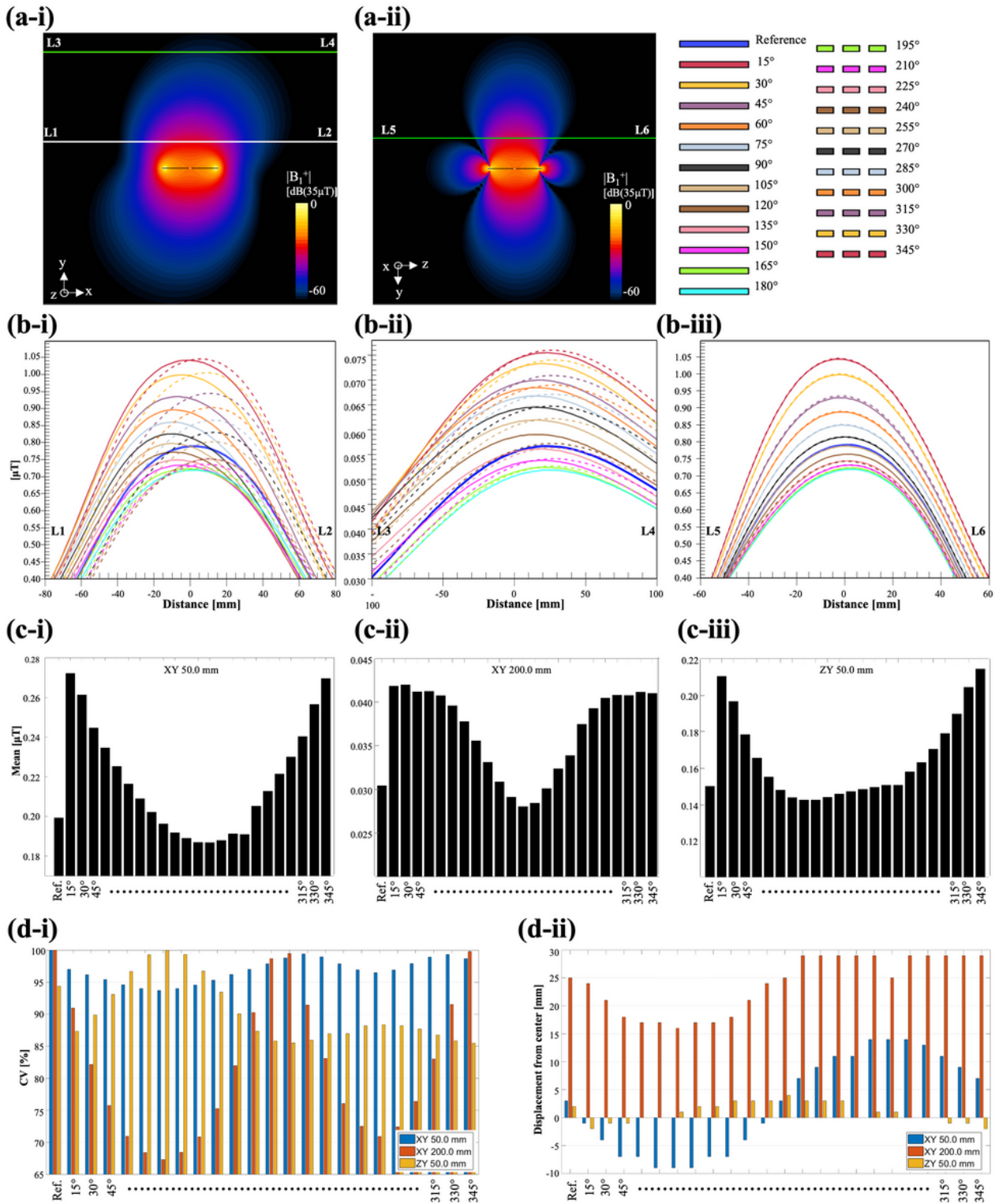


Figure 2

Computed $|B_1^+|$ field in empty space in (a-i) XY plane and (a-ii) YZ plane. (b-i) Plots of L1–L2 profile lines, (b-ii) L3–L4 profile lines, and (b-iii) L5–L6 profile lines, for all coil configurations. Statistical analysis of $|B_1^+|$ -field in empty space, showing mean values for line profiles (c-i) in XY plane, at 50 mm, (c-ii) in XY plane, at 200 mm, and (c-iii) in ZY plane, at 50 mm. (d-i) CVs for all tested coil configurations and line

profiles; values have been scaled based on the maximum for easier comparison. (d-ii) Focus of the field, computed based on displacement of maximum value from the center, for all line profiles.

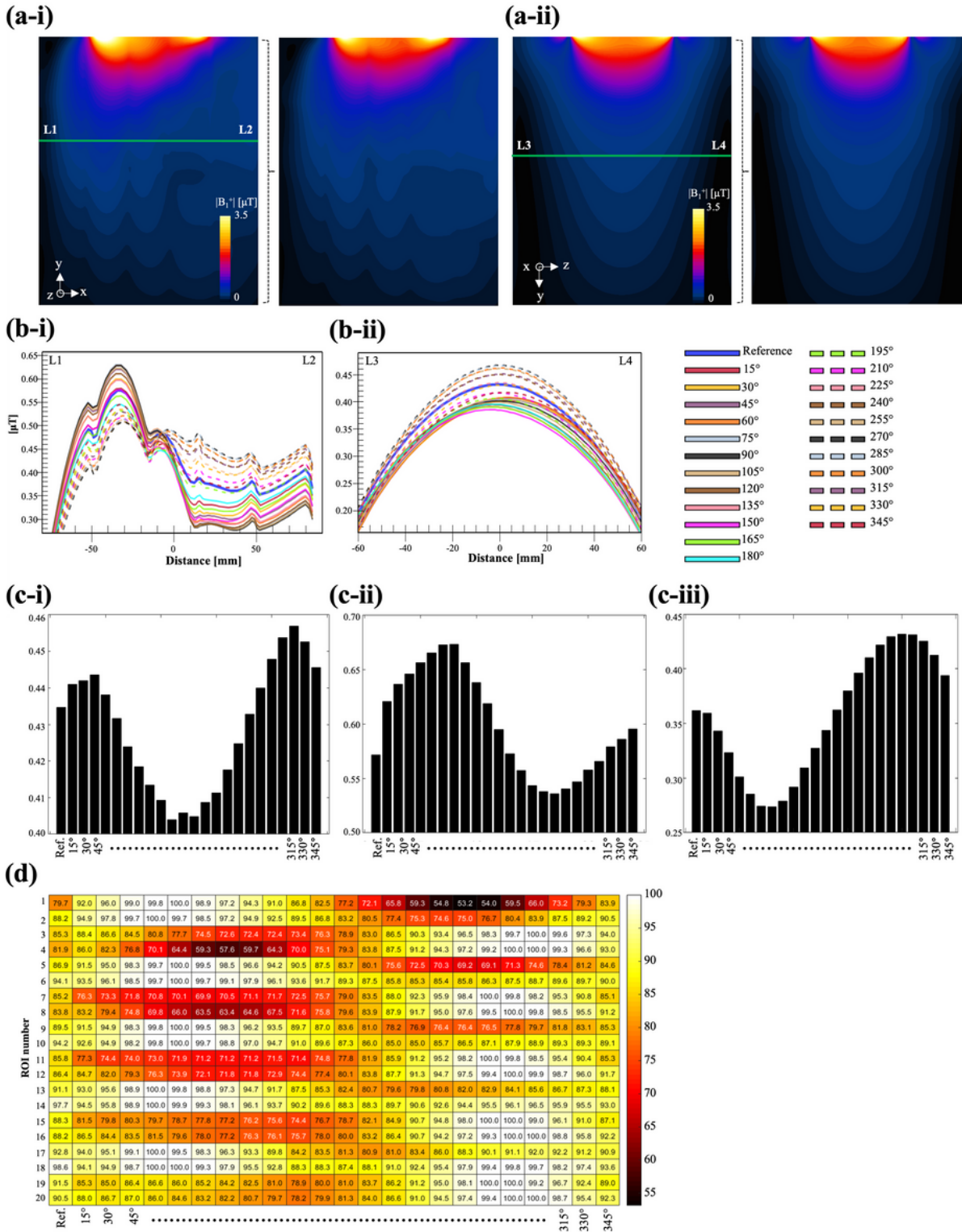


Figure 3

Computed $|B_1^+|$ field inside phantom in XY plane for (a-i) the reference coil and the coil with capacitor at 315° . The field in view in the YZ plane (a-ii) for the reference coil, and coil with capacitor at 315. (b-i) L1–

L2 line profile and (b-ii) L3–L4 line profile. (c-i) Mean values of $|B_1^+|$ field in the XY plane, (c-ii) CVs in the XY plane, (c-iii) mean values of $|B_1^+|$ field in ROI 8 for all tested coil configurations. (d-i) mean values in all ROIs of phantom for all tested coil configurations.

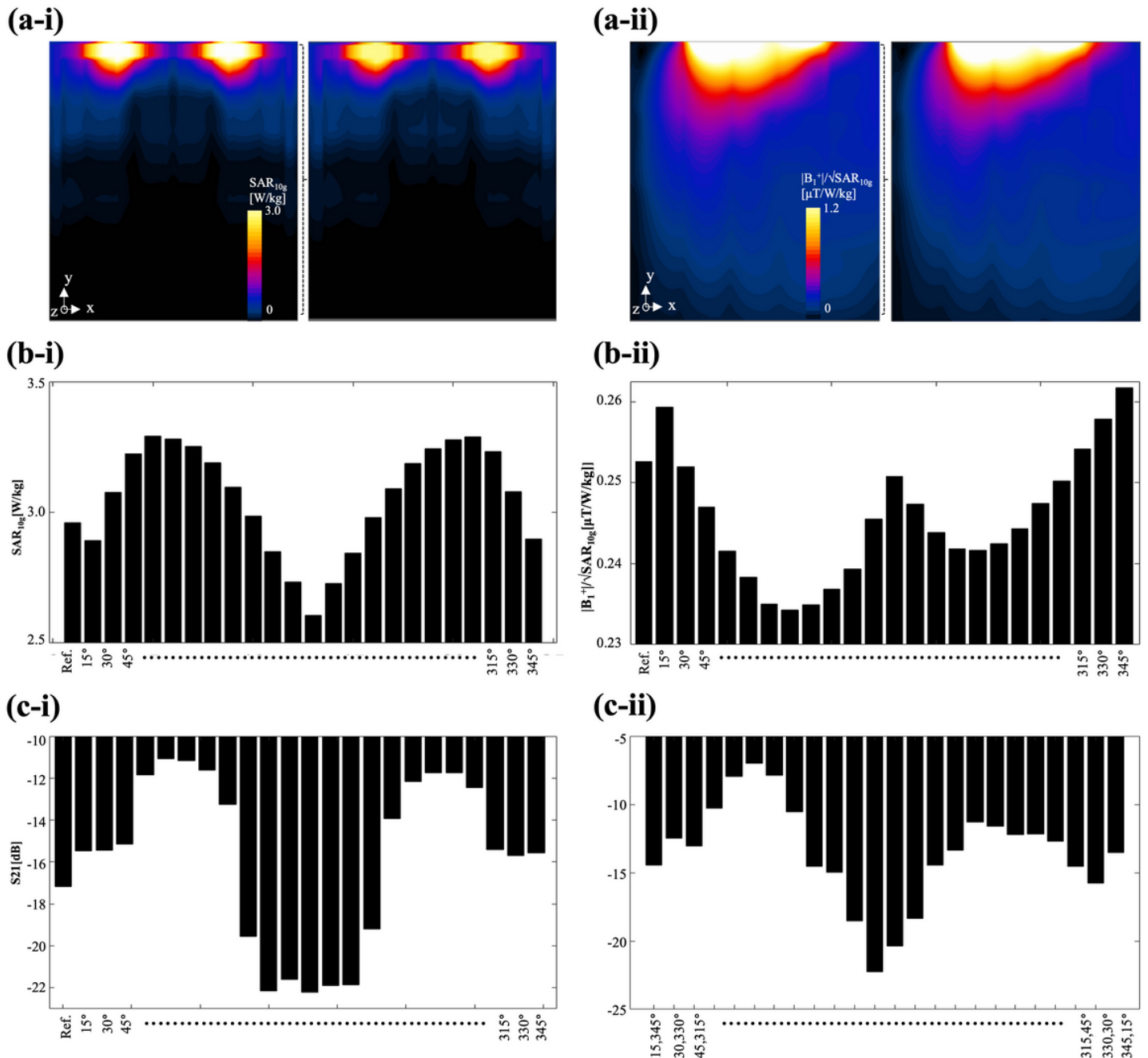


Figure 4

Computed SARs in XY plane for (a-i) reference coil, and coil with capacitor at position 180°. Normalized $|B_1^+|$ -field based on maximum SAR (a-ii) for the reference coil and coil with capacitor at position 345°. (b-i) Maximum SARs in phantom for all tested coil configurations, and (b-ii) mean values of normalized

$|B_1^+|/\text{SAR}_{\text{max}}$ field for all tested coil configurations. Coupling analysis of S21 parameters for (c-i) coils with identical configurations, and (c-ii) coils with different configurations.

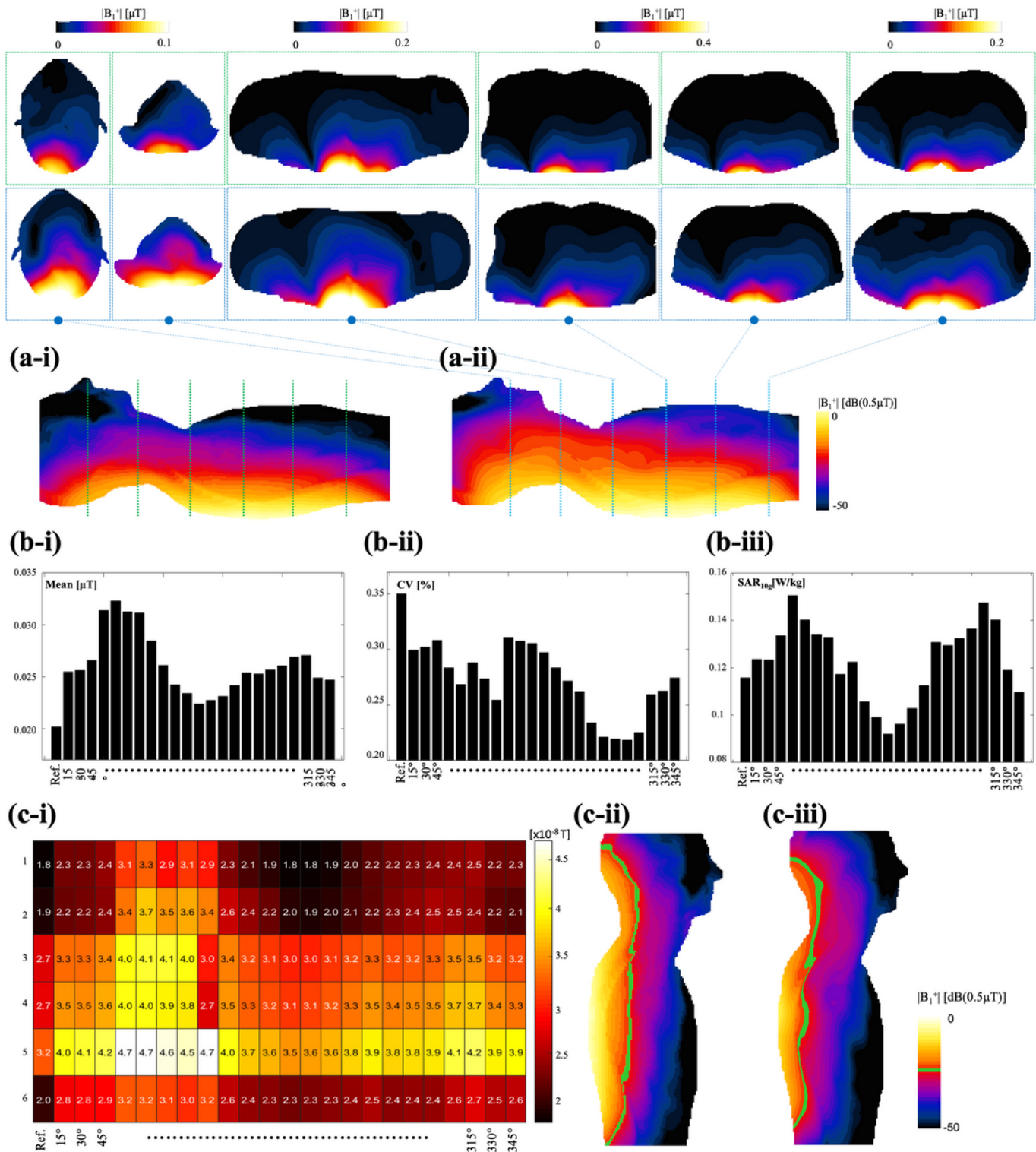


Figure 5

Computed $|B_1^+|$ field in XY plane for arrays of (a-i) reference coils, with details shown in top panel, and (a-ii) coil with capacitor at position 75° , with details shown in bottom panel. Statistics of computed $|B_1^+|$

field: (b-i) mean, (b-ii) CV, and (b-iii) maximum SAR_{10g} values for all tested coil configurations. (c-i) Mean values of $|B_1^+|$ field for all slices at coil center for all tested coil configurations. $|B_1^+|$ field in ZY plane for (c-ii) reference coil array, and (c-iii) optimized coil array, showing highlighted magnetic field.

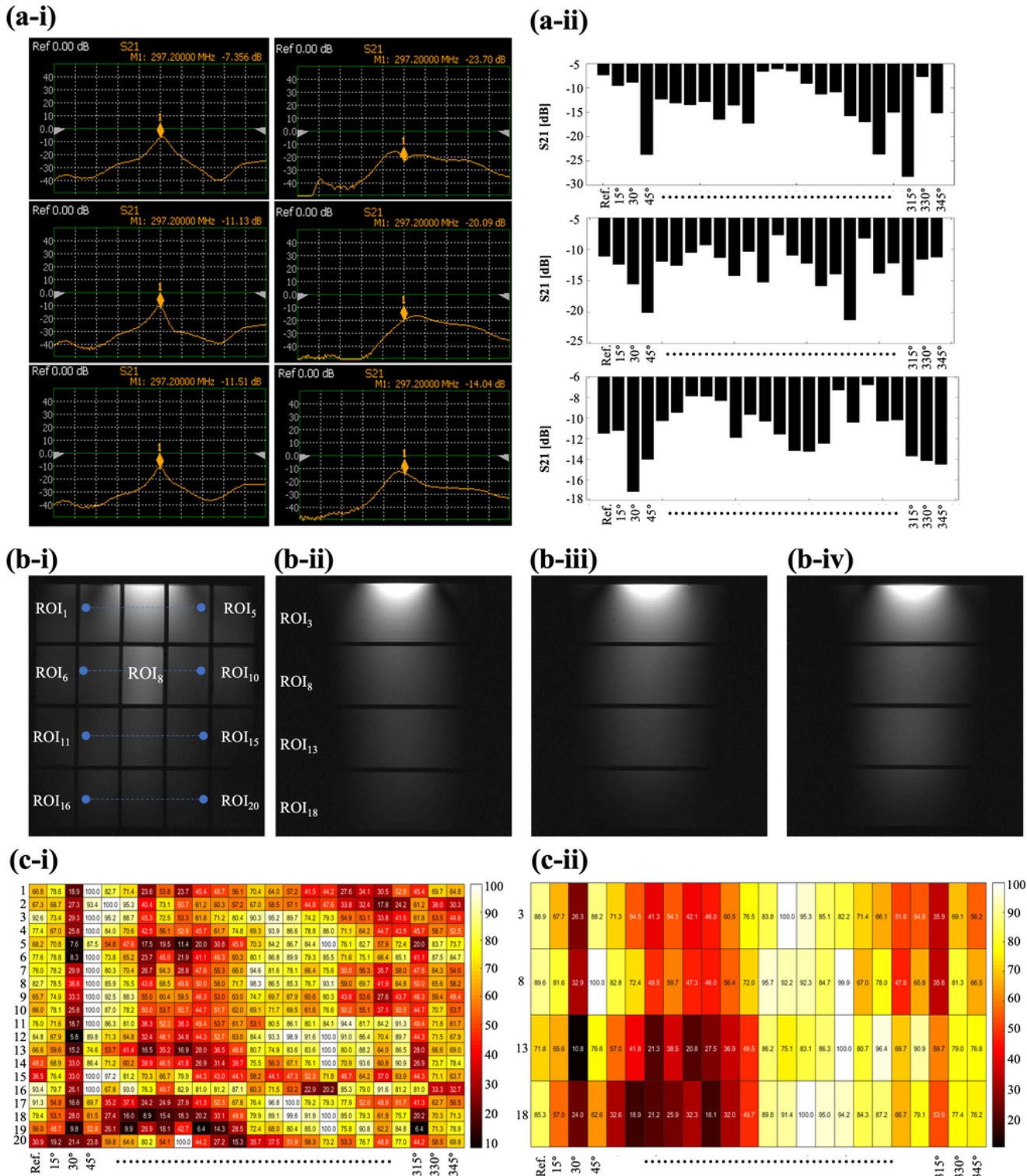


Figure 6

(a-i) S21 parameters from network analyzer for reference coil (left) and C45 (right), and (a-ii) S21 parameters for all tested coil configurations at 297.3 MHz, for coil separation distances of 65, 60, and 55 mm, shown in top, middle, and bottom panels, respectively. Acquired GRE MRI images in axial (b-i) and sagittal views, for (b-ii) reference coil, and coils with capacitors at (b-iii) 45° and (b-iv) 240°. Mean values for all ROIs and for all tested coil configurations in (c-i) axial and (c-ii) sagittal views.

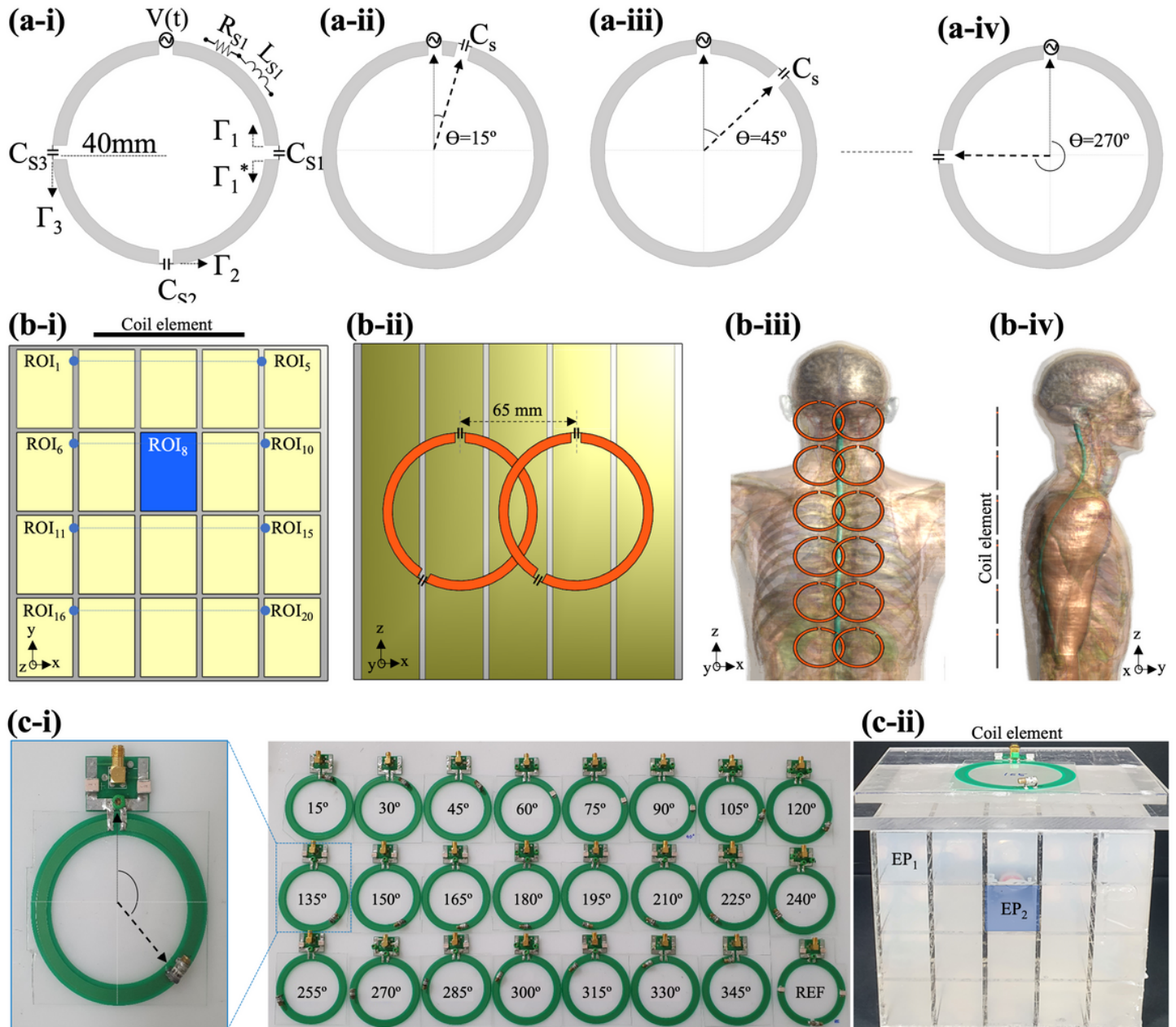


Figure 7

Visualization of concept of non-symmetric distributed RF coils, with (a-i) reference, and coils with capacitor positions at (a-ii) 15°, (a-iii) 45°, and (a-iv) 270°. Models for EM simulations involving (b-i) phantom, indicating position of each ROI, (b-ii) setup used for coupling analysis between two coils of the same type. Array consisting of 6 pairs of coils for human model, with spinal cord as the target, in (b-iii)

XZ plane and (b-iv) YZ plane. RF coils created for this study, showing (c-i) single coil with capacitor placed at 210° with corresponding matching circuit, and 24 coils, including reference coil, for coil combinations with capacitor positioned between 15° and 345° , in 15° intervals. (c-ii) ROI phantom with 20 ROIs, and location of coil on top for MRI imaging.